Energy & Environmental Science

ROYAL SOCIETY OF CHEMISTRY

PAPER

View Article Online
View Journal | View Issue

Cite this: *Energy Environ. Sci.*, 2026, **19**, 1331

Multidentate silane bridging for stable and efficient perovskite–organic tandem solar cells

Dong Zhang,[a] Baoze Liu,[a] Xue Wang,[ab] Qi Liu,[c] Danpeng Gao,*[a] Xianglang Sun,*[a] Xin Wu,[a] Zexin Yu,[a] Chunlei Zhang,[a] Ning Wang,[a] Yan Wang,[a] Nikhil Kalasariya,[d] Francesco Vanin,[a] Weidong Tian,[a] Shuai Li,[a] Jianqiu Gong,[a] Lina Wang,[a] Yang Bai,[e] Shuang Xiao,[f] Bo Li,[g] Martin Stolterfoht,[d] Xiao Cheng Zeng,*[c] Shangfeng Yang *[b] and Zonglong Zhu *[ahi]

Perovskite–organic tandem solar cells (POTSCs) offer significant advantages over other perovskite-based tandem architectures owing to their straightforward processing and broad tuneability. However, the interfacial energetics disorder and resulting heterogeneous photoactive phase in wide bandgap perovskite subcells significantly undermine their long-term stability. Here, we develop a multidentate anchoring-bridging strategy that establishes a periodic passivating array that coordinates with dangling Pb^{2+} on the perovskite surface to reduce vacancy-mediated halide migration. The network with fluorinated chains reconfigures the interfacial dielectric landscape, significantly increasing the migration activation barrier for halide vacancies at the perovskite/electron transport layer interface, suppressing ion migration and significantly enchancing longevity. Poly-FPTS-treated tandem devices delivered a power conversion efficiency (PCE) of 26.5%, with a high open-circuit voltage of 2.178 V. A steady-state certified efficiency of 25.1% was achieved in Japan Electrical Safety & Environmental Technology Laboratories (JET), as reported in Solar Cell Efficiency Tables (version 65). Under continuous 1-sun illumination at the maximum power point (ISOS-L-1I protocol), these devices retained 92% of their initial efficiency after 1000 hours, and they exhibited an efficiency loss $< 5\%$ after 1056 hours of light–dark cycling (ISOS-LC-1). This work reveals the importance of treating the top perovskite/ETL contact for commercializing perovskite–organic tandem solar cells.

Received 21st October 2025,
Accepted 22nd January 2026

DOI: 10.1039/d5ee06253e

rsc.li/ees

Broader context

Perovskite–organic tandem solar cells (POTSCs) offer a promising path to next-generation photovoltaics, combining the high efficiency of perovskites with the processing advantages and spectral tunability of organic materials. Despite the enormous potential of POTSCs, their commercialization is impeded by insufficient operational stability required for practical applications, primarily due to ion migration and interfacial degradation at the top perovskite subcell. In this study, we develop a multidentate anchoring–bridging strategy that constructs a periodic fluorinated passivating network coordinating with undercoordinated Pb^{2+}, suppressing vacancy-mediated halide migration, and restructures the local dielectric environment. The resulting devices achieve a remarkable power conversion efficiency of up to 26.5% and exhibit exceptional operational stability, retaining 92% of their initial efficiency after 1000 hours of continuous illumination. This study underscores the critical role of top interface engineering in achieving high efficiency and longevity, providing a viable pathway toward commercializing perovskite–organic tandem photovoltaics.

[a] *Department of Chemistry, City University of Hong Kong, Hong Kong SAR, P. R. China. E-mail: dp.gao@cityu.edu.hk, zonglzhu@cityu.edu.hk, sxl@hust.edu.cn*
[b] *Department of Materials Science and Engineering, University of Science and Technology of China, Hefei, Anhui, P. R. China. E-mail: sfyang@ustc.edu.cn*
[c] *Department of Materials Science & Engineering, City University of Hong Kong, Hong Kong SAR, P. R. China. E-mail: xzeng26@cityu.edu.hk*
[d] *Department of Electronic Engineering, The Chinese University of Hong Kong, Hong Kong SAR, P. R. China*
[e] *School of Materials Science and Engineering, Beijing Institute of Technology, Beijing, P. R. China*
[f] *Center for Advanced Material Diagnostic Technology and College of Engineering Physics, Shenzhen Technology University, Shenzhen, Guangdong, P. R. China*
[g] *Department of Materials Science & Engineering, Central South University, Changsha, Hunan, P. R. China*
[h] *Hong Kong Institute for Clean Energy, City University of Hong Kong, Hong Kong SAR, P. R. China*
[i] *City University of Hong Kong Shenzhen Research Institute, Shenzhen, Guangdong, P. R. China*

Introduction

Perovskite-based tandem solar cells have achieved remarkable power conversion efficiencies (PCEs), positioning them as promising candidates for commercialization in sustainable energy applications.[1–7] Among various tandem architectures, perovskite–organic tandem solar cells (POTSCs) offer distinctive advantages, such as low-cost solution processability and flexible substrate compatibility.[8–16] However, their practical application is limited by insufficient operational stability.[17–22] This instability primarily stems from halide vacancy defects-assisted ion migration within wide-bandgap perovskite bottom subcells, which predominantly occur at interfaces and contribute significantly to device degradation.[23–36] Central to this deterioration process are the uncoordinated Pb^{2+} ions on the perovskite surface, which act as highly active defect sites, promote the hopping tendency of neighbouring halide vacancies, and exacerbate lattice relaxation, thereby accelerating the generation and aggregation of halide ions.[37–44] While conventional small-molecule passivation agents can partially passivate Pb dangling bonds, their monodentate coordination introduces steric hindrance, impeding the passivation of adjacent Pb defects and resulting in a weak interaction.[45–51] Therefore, exploring strategies that saturate dangling Pb sites to suppress interfacial ion migration is crucial for advancing POTSCs.

Herein, we developed a multidentate anchoring-bridging strategy through the *in situ* coupling of (3,3,3-trifluoropropyl) trimethoxy silane (FPTS) at the perovskite surface, effectively homogenizing interfacial energetics and suppressing mobile ion migration, ultimately affording efficient and stable POTSCs. The coupling FPTS network consists of periodic Pb–O coordination arrays that saturate exposed Pb sites, thereby achieving interfacial dielectric reconstruction, homogenizing surface potential and suppressing interfacial phase aggregation. Using this approach, we fabricated devices with a PCE of 26.5% in the reverse scan and 25.8% in the forward scan (steady-state certified efficiency 25.1% in JET), with a high open-circuit voltage of 2.178 V and 2.169 V, respectively. The optimized devices exhibited exceptional illumination stability with efficiency loss less than 8% of their initial efficiency after 1000-hour maximum power point (MPP) tracking under 1-sun illumination (25 °C, ISOS-L-1I). Additionally, they maintained 95% of their initial efficiency after 1056 hours of continuous light–dark cycling (ISOS-LC-1).

Results and discussion

Suppression of ion migration

Effective multidentate anchoring-bridging passivation necessitates ligands exhibiting uniform coordination distances to exposed Pb^{2+} ions on perovskite surfaces, preserving disordered packing while facilitating unimpeded charge transfer. To comprehensively address these criteria, we adopted a molecule with a propyl silane motif having three methoxy groups and a terminal $–CF_3$ moiety (Fig. 1a). The proposed coupling reaction mechanism is shown in Fig. S1 (SI),[52–54] corroborated by the ^{1}H-nuclear magnetic resonance (NMR) spectra (Fig. S2, SI). Configuration analysis (Fig. 1b) reveals that the O–Si–O bond distance (~2.19 Å) closely matches one-third of the Pb–Pb lattice spacing (~6.3 Å) in FACs-based perovskites (FA: formamidinium; Cs: cesium), thereby facilitating oxygen lone-pair coordination with Pb^{2+} to form periodic arrays. The $–CF_3$ group with potent electronegativity and high polarity amplifies charge transfer efficiency and engenders interfacial hydrophobicity.[55–59]

Multidentate anchoring-bridging was validated through Fourier transform infrared (FTIR) spectroscopy (Fig. S3, SI). Pre-thermal annealing spectra displayed characteristic CF_3 (1280 cm^{-1}) peaks. Post-thermal annealing, however, a broad Si–O–Si (1099 cm^{-1}) vibration emerged, confirming the formation of a crosslinked siloxane network on the perovskite surface.[60–62] Concurrent X-ray photoelectron spectroscopy (XPS) unveiled progressive upward shifts in Pb 4f binding energy by 0.06 eV in FPTS-treated films and 0.13 eV in poly-FPTS-treated films compared to the untreated films (Fig. 1c). Mirroring this trend, concomitant shifts in I 3d and Br 3d spectra signalled diminished electron density around halogens, characteristic of Pb–O coordination (Fig. S4, SI). The structural integrity was maintained, with nearly unchanged morphology, optical properties and crystal quality (Fig. S5–S8, SI).

We then analyzed the halide vacancy energetics in three systems using density functional theory (DFT) calculations (VASP 6.4, Fig. S9, SI). Poly-FPTS films exhibited a markedly elevated formation energy (E_f) of 2.10 eV (V_I) and 1.93 eV (V_{Br}), surpassing FPTS (2.07 eV; 1.38 eV) and untreated films (2.05 eV; 1.03 eV) (Fig. 1d). Migration activation energy (E_a) of halide vacancies exhibited the same trend, with iodide vacancy activation energies of 0.41 eV (untreated films), 0.58 eV (FPTS-treated films) and 0.63 eV (poly-FPTS-treated films). Bromide vacancy migration activation energy also increased from 0.32 eV to 0.61 eV (FPTS films) and 0.79 eV (poly-FPTS films) (Fig. 1e). These results reveal that coupled FPTS exhibited improved potential for suppressing defect-mediated ion migration, compared to single-site passivation.

Supporting simulations corroborated that the efficiency decay is proportional to mobile ion density (Fig. S10, SI).[63,64] Experimentally, bias-assisted charge extraction (BACE) quantified the mobile ion concentrations n_{ion} of 1.28×10^{17} cm^{-3} (control) in contrast to 9.10×10^{16} cm^{-3} (FPTS) and 4.15×10^{16} cm^{-3} (poly-FPTS) (Fig. 1f and Note S1, SI). This downward trend is consistent with space-charge-limited current (SCLC) measurements, which show attenuated trap densities, whilst Mott–Schottky analysis revealed suppressed ion-induced field screening (Fig. S11–S13 and Note S2, SI),[63] collectively underscoring mobile ion immobilization *via* enhanced Pb-coordination.

We further investigated ion migration activation energies (E_a) of the three systems through temperature-dependent conductivity measurement. Poly-FPTS-treated perovskite films exhibited an increased activation energy E_a of 0.773 eV compared with 0.666 eV (FPTS films) and 0.204 eV (untreated films) (Fig. 1g). Moreover, calculated migration rates fell by 10 orders of magnitude relative to untreated films (Fig. S14 and S15 and Note S3, SI). Practical verification was performed by

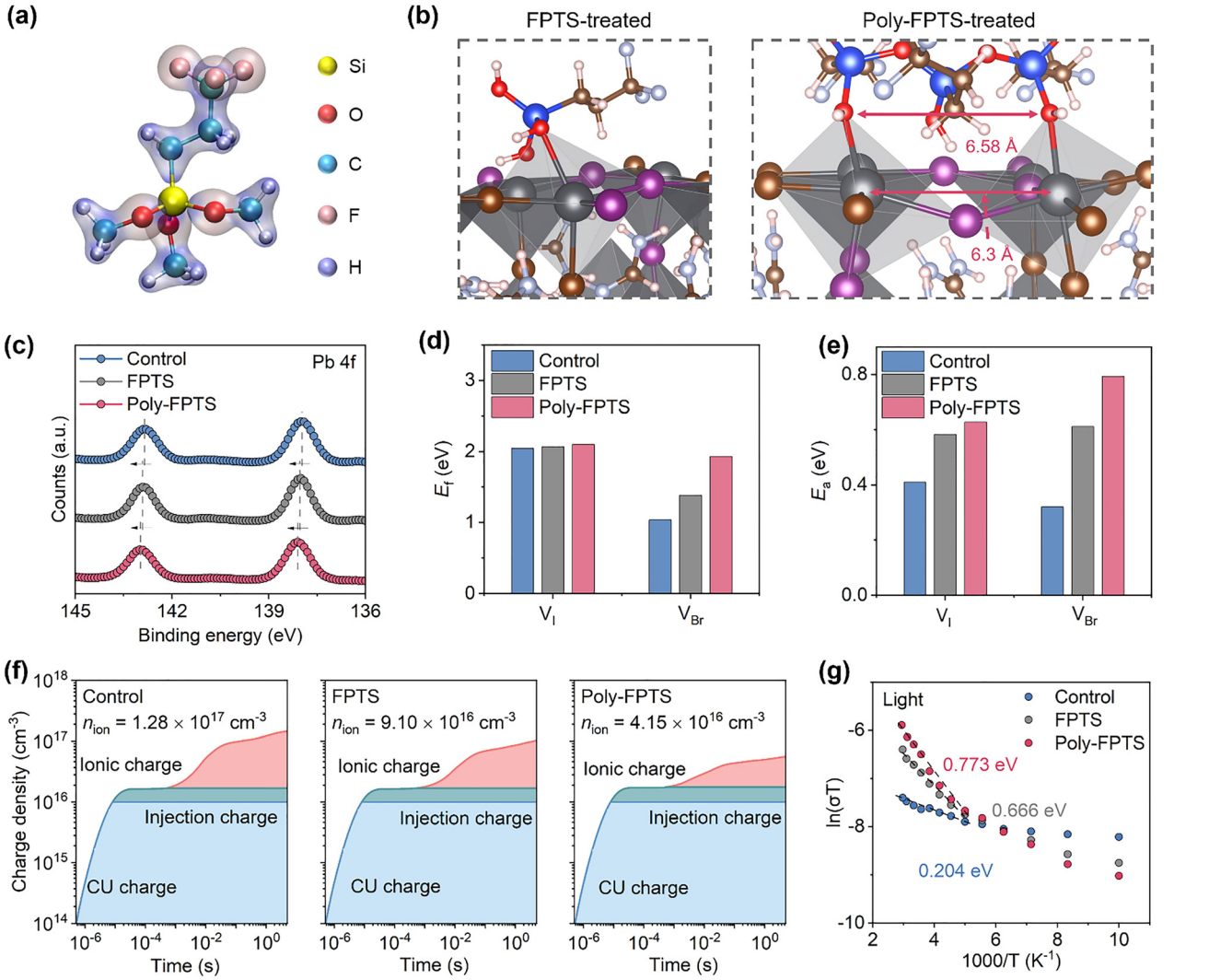

Fig. 1 Suppression of ion migration. (a) The molecular structure of (3,3,3-trifluoropropyl) trimethoxy silane (FPTS). (b) DFT calculated untreated, FPTS, and poly-FPTS configurations on perovskite films. To more clearly illustrate the surface interactions, the FPTS molecules in the computational model are presented in their hydrolysed silanol (Si–OH) form. (C) Pb 4f XPS spectra of untreated, FPTS, and poly-FPTS treated perovskite films. (d and e) Calculated formation energy (d) and migration energy (e) of V_I and V_{Br} in untreated, FPTS, and poly-FPTS on perovskite films. (f) BACE measured mobile ion density in untreated, FPTS-treated, and poly-FPTS-treated films. (g) The ion migration activation energy (E_a) of the untreated, FPTS, and poly-FPTS treated devices under light conditions.

time-of-flight secondary ion mass spectrometry (ToF-SIMS). After 200 h of illumination, the untreated devices showed severe halide electrode accumulation, while the poly-FPTS-treated devices maintained the initial halogen distribution (Fig. S16–S18, SI). The multidentate anchoring-bridging strategy achieved through coupled FPTS significantly reduces vacancy defect sites and migration pathways, suppressing interfacial aggregation.

Optoelectronic properties evolution of perovskite films

To investigate the evolution of optoelectronic properties following poly-FPTS modulation, we probed perovskite energetics using ultraviolet photoelectron spectroscopy (UPS) and Kelvin probe force microscopy (KPFM). UPS revealed a reduced mean work function (W_F) for poly-FPTS-treated films (5.04 eV) *versus* untreated counterparts (5.13 eV), indicating improved interfacial energy alignment (Fig. S19, SI). Crucially, as shown in Fig. 2a–c, KPFM surface potential imaging revealed markedly narrower distributions in poly-FPTS films (30.2 ± 16.2 mV) compared to controls (34.6 ± 18.2 mV). After 200-hour illumination in a N_2 chamber, poly-FPTS films maintained exceptional homogeneity (36.0 ± 19.3 mV), while untreated films showed pronounced heterogeneity (63.1 ± 25.6 mV), suggesting poly-FPTS-induced electrical stabilization. The attenuated inhomogeneity stems from suppressed defect-induced ion accumulation during illumination aging,[23–26,65] where localized defects and energetic disorder, primary drivers of halide mobility, are inhibited by multidentate passivation.

We quantified the surface potential differentials (ΔCPD = CPD_{GB} -CPD_{GI}) between the grain boundaries (GBs) and

interiors (GI) across six sections (Fig. S20, SI).[66–70] Poly-FPTS films exhibited restrained initial ΔCPD (25.0 ± 2.13 mV), with minimal aging-induced increases (26.3 ± 6.41 mV). Untreated films, conversely, suffered dramatic ΔCPD expansion, from 31.8 ± 7.11 mV to 50.4 ± 6.82 mV (Fig. 2d), revealing rampant energetic disorder. This significant reduction highlights the

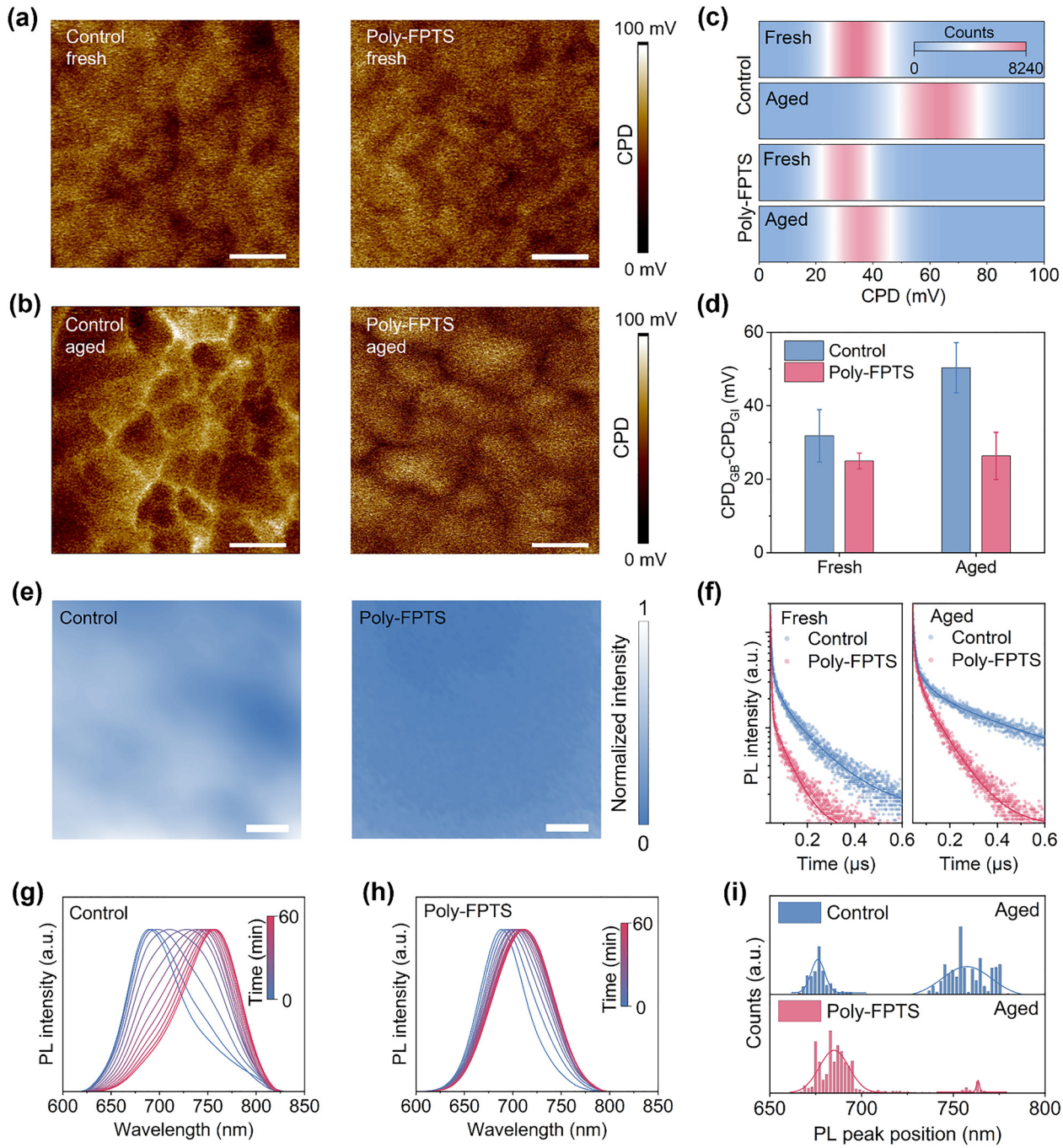

Fig. 2 Optoelectronic properties evolution of perovskite films. (a) KPFM of perovskite films without and with poly-FPTS treatment. The scale bar is 500 nm. (b) KPFM of perovskite films without and with poly-FPTS treatment aged after 200 hours of illumination using a white LED. The scale bar is 500 nm. (c) The contact potential difference (CPD) distribution of fresh and aged perovskite films without and with poly-FPTS treatment. The distribution was fitted by a Gaussian function. (d) Surface potential difference (ΔCPD = CPD_{GB} − CPD_{GI}) between the grain boundaries (GBs) and grain interior (GI) of fresh and aged perovskite films without and with poly-FPTS treatment. (e) PL mapping of fresh and aged perovskite/ETL films without and with poly-FPTS treatment. The scale bar is 1 μm. (f) TRPL spectrum of perovskite/ETL films without and with poly-FPTS treatment. The incident excitation light entered from the ETL side. The lifetimes for each trace were fitted with a biexponential decay. (g and h) *In situ* PL spectrum evolution of perovskite films without (g) and with (h) poly-FPTS treatment under continuous aging. The encapsulated films are exposed to 480 nm laser light for 60 minutes. (i) PL mapping of perovskite films without (top) and with (bottom) poly-FPTS treatment after 200 hours of illumination aging.

efficacy of poly-FPTS in homogenizing surface potential and mitigating the driving force for ion migration. Collectively, these metrics demonstrate how multidentate anchoring-bridging homogenizes interfacial energetics to facilitate charge transfer.

Interfacial charge extraction was evaluated *via* photoluminescence (PL) on perovskite/electron transport layer (ETL) stacks. Regarding uniformity, poly-FPTS-treated films exhibited uniformly quenched PL intensity, indicating improved and spatially consistent electron extraction, which starkly contrasts with the patchy emission of the controls (Fig. 2e). The robustness of this interface modulation was further investigated using steady-state photoluminescence (PL). For fresh films, the PL intensity decreased after poly-FPTS treatment, indicating enhanced electron extraction in contrast to untreated films (Fig. S21, SI). After illumination aging, the poly-FPTS-treated films maintained similar emission spectra, whereas the control films showed a significant increase in PL intensity and a redshift, highlighting the durability of the poly-FPTS passivation layer. This is also corroborated by time-resolved PL spectra of perovskite films with transporting layers before and after illumination aging (Fig. 2f), where the carrier lifetime in poly-FPTS-modified films rose from 28.2 ns (fresh) to 61.5 ns (aged). In comparison, untreated films deteriorated from 82.2 ns (fresh) to 135.8 ns (aged) (Table S1, SI). These dynamics confirm that poly-FPTS modification overcomes the out-of-plane charge transport barrier by alleviating the ion-induced field screening effect, thereby enhancing carrier extraction.[63,71] In addition to the measurements under open circuit conditions, we also characterized the devices using transient photocurrent (TPC) under short-circuit conditions. The results indicated that the characteristic decay time τ decreased from 1.25 μs for the untreated perovskite devices to 0.74 μs for the poly-FPTS-treated devices, confirming that the passivation strategy enhances electron extraction from the perovskite to the ETL (Fig. S22 and Note S4, SI).

In situ PL spectroscopy tracked macroscopic phase evolution under continuous 480-nm laser illumination. Untreated films showed progressive PL redshift and peak splitting, signifying halide segregation as carriers cascaded into lower-energy iodide-rich domains. Spectral centroid analysis quantified this degradation: untreated films exhibited pronounced bathochromic shifts within 60 minutes (Fig. 2g). However, poly-FPTS-treated films maintained the homogenous perovskite phase, withstanding intense illumination (Fig. 2h). The PL mapping in Fig. 2i validated uniform suppression of phase segregation across poly-FPTS-treated samples, corroborated with the homogeneous surface potential above (Fig. S23, SI). After 200-hour illumination aging, poly-FPTS-treated films retained original emission profiles, while untreated films showed severe phase separation. We attribute this photostability to modified defect-mediated halide migration dynamics.

Performances of POTSCs

Building on the improvement of a multidentate anchoring-bridging strategy on perovskite optoelectronic properties, we studied a device configuration consisting of indium tin oxide (ITO)/NiO_x/[2-(3,6-dimethyl-9*H*-carbazol-9-yl)ethyl]phosphonic Acid (Me-2PACz)/$FA_{0.8}Cs_{0.2}Pb(I_{0.55}Br_{0.45})_3$/poly-FPTS/$C_{60}$/2,9-dimethyl-4,7-diphenyl-1,10 phenanthroline (BCP)/silver (Ag). Fig. S24 and S25 (SI) show the current density–voltage (J–V) curves of untreated, FPTS-treated and poly-FPTS-treated PSCs. The untreated devices exhibit a maximum PCE of 17.33%, with a V_{OC} of 1.296 V, a J_{SC} of 16.59 mA cm^{-2}, and a FF of 80.60%. The introduction of poly-FPTS achieves a significant improvement, as shown in Table S2 (SI). The poly-FPTS-modified device produces a champion PCE of 19.37%, with a V_{OC} of 1.366 V, a J_{SC} of 16.83 mA cm^{-2}, and a FF of 84.24%. In addition, the performance of poly-FPTS-modified devices at various concentrations is summarized in Fig. S26 and Table S3 (SI), as well as the optimal concentration performance of perovskite devices with different bandgaps (Fig. S27 and Table S4, SI).

Advancing to tandems, we proceeded to fabricate POTSCs with the architecture of ITO/NiO_x/Me-2PACz/$FA_{0.8}Cs_{0.2}Pb(I_{0.55}Br_{0.45})_3$/poly-FPTS/$C_{60}$/BCP/gold (Au)/$MoO_x$/[2-(9*H*-Carbazol-9-yl)ethyl]phosphonic acid (2PACz)/PM6:PM7:Y6:$PC_{61}BM$/C_{60}/BCP/Ag (Fig. 3a). The organic subcell employed a quaternary bulk-heterojunction (BHJ) active layer (PM6: PM7: Y6: $PC_{61}BM$) in a ITO/MoO_x/BHJ/C_{60}/BCP/Ag stack, achieving a PCE of 18.02% (V_{OC} of 0.843 V, J_{SC} of 27.88 mA cm^{-2} and FF of 76.67%) (Fig. S28–S30 and Table S5, SI) and exhibiting excellent stability (Fig. S31, SI). As shown in Fig. 3b and 3c, and Tables S6–S8 (SI), by integrating these high-performance subcells, the tandem device achieved a PCE of 26.51% (V_{OC} = 2.178 V, J_{SC} = 14.52 mA cm^{-2}, FF = 83.83%). This significantly surpasses the PCE of the untreated device. Meanwhile, negligible hysteresis and narrow PCE distribution were observed in Fig. S32 and S33 (SI). To assess the practical potential of our surface-control strategy, we also fabricated devices with a larger active area of 1.05 cm^2. The champion device exhibited a PCE of 24.52%, demonstrating the robustness of the strategy upon scaling (Fig. S34 and Table S9, SI).

Cross-sectional SEM imaging confirmed optimized layer thicknesses (~400 nm perovskite, ~130 nm BHJ; Fig. S35, SI), enabling balanced light absorption and current matching, a conclusion supported by external quantum efficiency (EQE) spectra yielding a matched J_{SC} of 14.53 mA cm^{-2} (Fig. 3d). As shown in Fig. 3e, stable power output (SPO) measurements at MPP revealed consistent performance for poly-FPTS-treated devices, whereas untreated devices exhibited gradual degradation. Encouraged by the exceptional performance, we certified our tandem solar cells through an accredited independent PV calibration laboratory (Japan Electrical Safety & Environmental Technology Laboratories, JET), confirming a certified stabilized PCE of 25.1% after 5 minutes of MPP tracking in ambient conditions without encapsulation (Fig. S36, SI). This PCE has been included and published in the solar cell efficiency tables (version 65).[72]

To elucidate the origin of the performance enhancement, we conducted statistical analyses on the photovoltaic parameters of 24 individual devices. The PCE improvements for POTSC

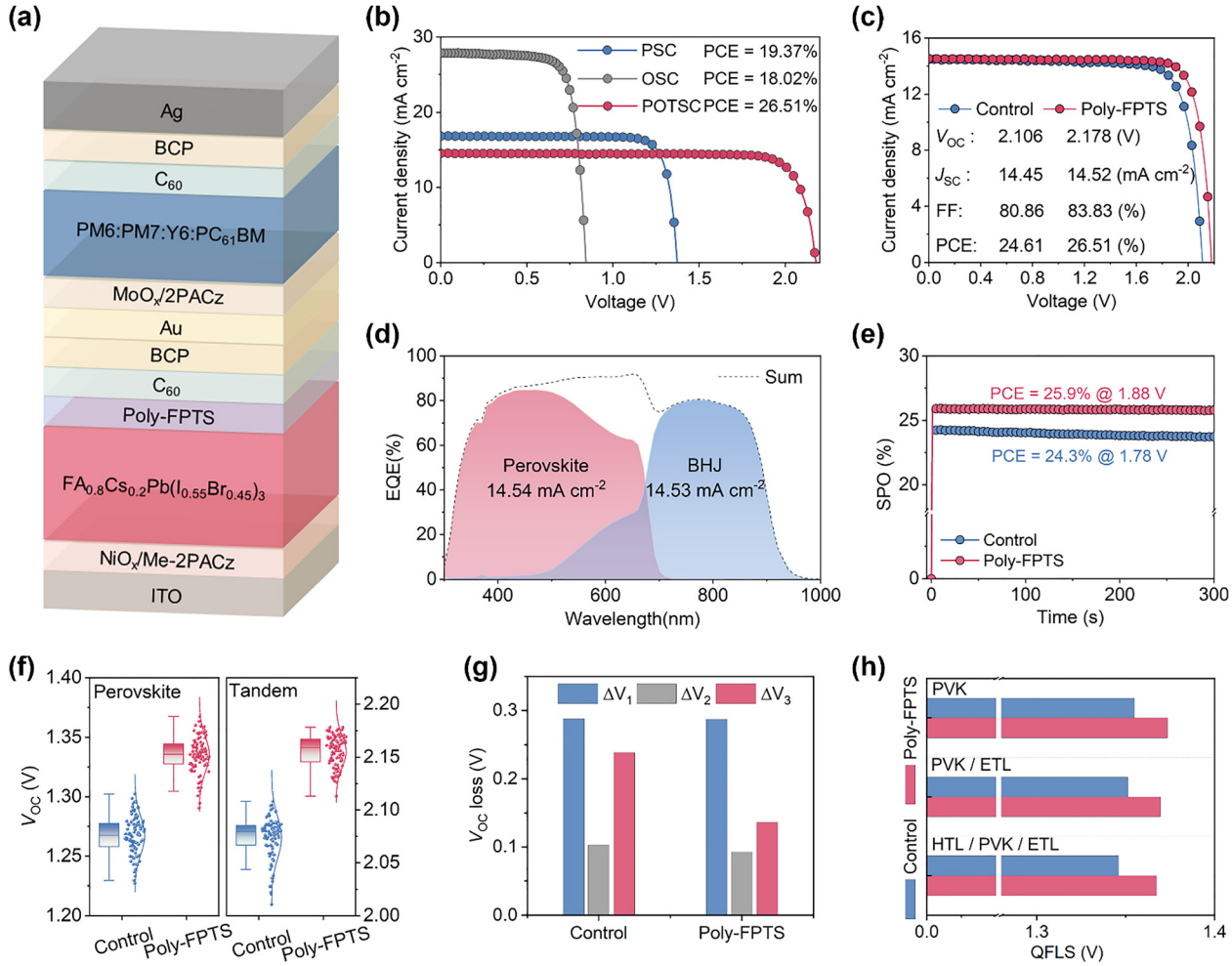

Fig. 3 The performances of POTSCs. (a) Schematic structure of the monolithic perovskite–organic tandem solar cells. (b) *J*–*V* curves of the champion perovskite solar cell (PSC), organic solar cell (OSC), and POTSC. (c) *J*–*V* curves of the champion POTSC without and with poly-FPTS treatment. (d) EQE spectra of the perovskite and BHJ subcells in champion POTSC. (e) Stable power output (SPO) of POTSCs without and with poly-FPTS treatment. (f) V_{OC} distribution of PSCs and POTSCs without and with poly-FPTS treatment. (g) V_{OC} loss analysis of untreated and poly-FPTS-treated PSCs. (h) QFLS analysis of untreated and poly-FPTS-treated perovskite films with different stacks of PVK, PVK/ETL, and HTL/PVK/ETL.

devices are mainly attributed to the increased V_{OC} and FF after incorporating poly-FPTS, as shown in Fig. S37 and Table S10 (SI). Notably, the V_{OC} increment contributes more significantly to the PCE augmentation for both POTSCs and PSCs devices, with contribution rates of 47.3% and 46.6%, respectively, which improved from an average V_{OC} of 1.276 V (without poly-FPTS) to 1.346 V (with poly-FPTS) for POTSCs and an average V_{OC} of 2.07 V (without poly-FPTS) to 2.158 V (with poly-FPTS) for PSCs, as shown in Fig. 3f. Voltage loss analysis was then conducted.[71] Fig. S38 and S39 (SI) show that the poly-FPTS-treated device demonstrates a 0.55% EQE-EL efficiency at device J_{SC} compared to 0.015% of untreated perovskite under the same conditions. The V_{OC} loss was quantitatively analyzed based on the detailed balance theory.[73] The detailed analysis and loss results are shown in Fig. 3g, Note S5, and Table S11 (SI). Notably, the ΔV_3 value declines from 238 mV to 136 mV after poly-FPTS treatment, implying effective suppression of non-radiative recombination. In addition, quasi-Fermi level splitting (QFLS) calculations derived from photoluminescence quantum yield (PLQY) measurements across different film stacks: neat perovskite, perovskite/ETL, and hole transport layer (HTL)/perovskite/ETL, revealed reduced interfacial voltage losses (Fig. 3h). The poly-FPTS-treated devices showed an elevated QFLS, with a V_{OC} of 1.373 V *versus* 1.355 V for PVK film, 1.369 V *versus* 1.351 V for PVK/ETL film, and 1.367 V *versus* 1.346 V for HTL/PVK/ETL film, respectively. These outcomes reflect the suppression of non-radiative recombination and the favourable QFLS at the perovskite/ETL interface, both of which are critical for maximizing photovoltaic performance.

Stability of POTSCs

To assess the long-term stability of POTSCs, we subjected untreated and poly-FPTS-treated POTSCs to 1000-hour MPP tracking under ISOS-L-1I protocols (1-sun illumination, room temperature, N_2 atmosphere; Fig. 4a).[74,75] Remarkably, poly-FPTS-treated devices retained 92% of their initial efficiency

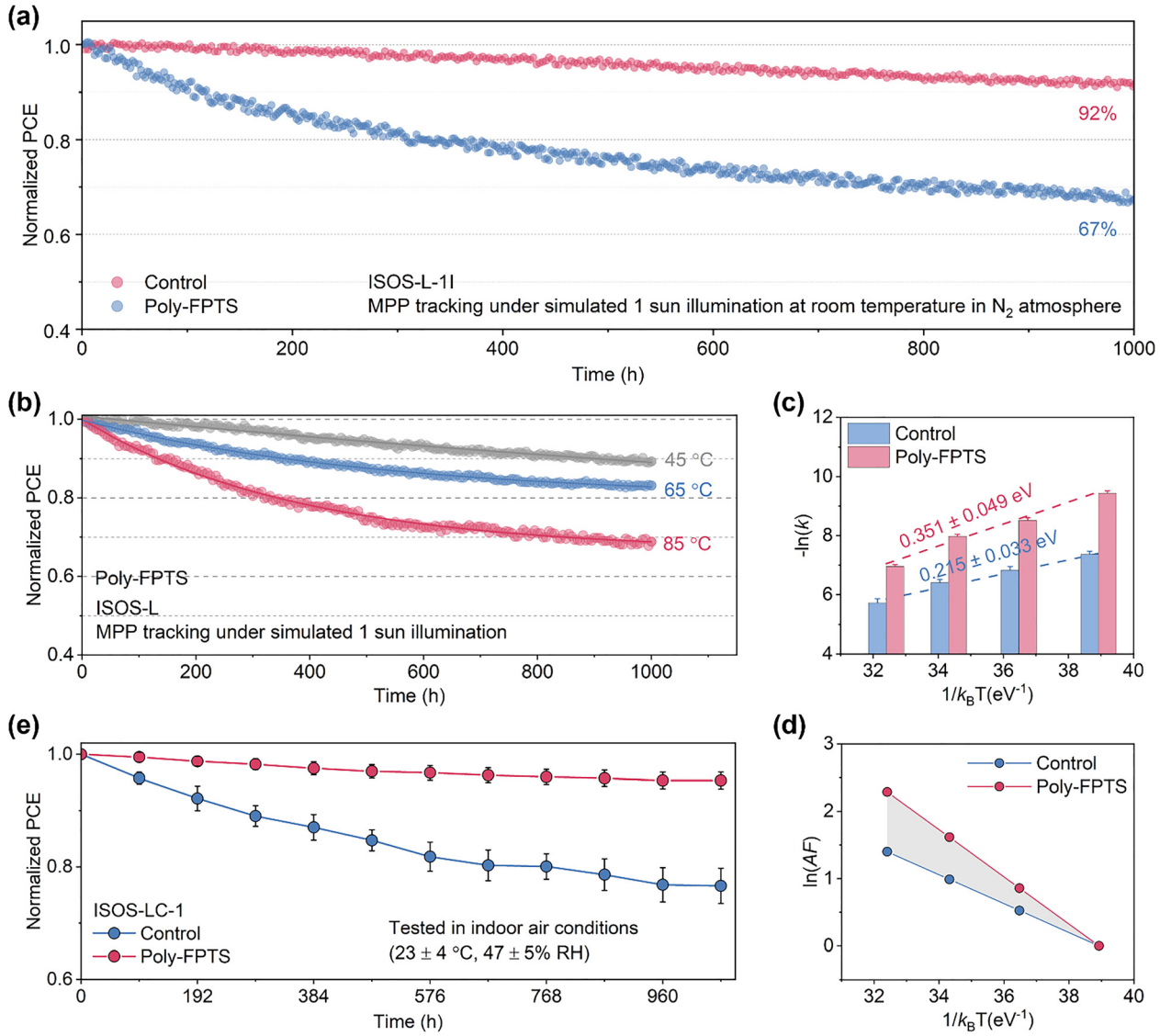

Fig. 4 The stability of POTSCs. (a) Continuous MPP tracking of the untreated and poly-FPTS-treated POTSCs under simulated 1-sun illumination in a N_2-filled chamber without temperature control (ISOS-L-1I). (b) Operational stability of poly-FPTS-treated POTSCs operating at 25 °C, 45 °C, 65 °C, 85 °C (ISOS-L). The encapsulated devices were held at their MPP under simulated 1-sun illumination. The solid lines are a bi-exponential fit to the data. (c) Natural logarithm of slow degradation rate (k_{slow}) *versus* $1/k_BT$ obtained from biexponential fits, where k_B is Boltzmann's constant and T is aging temperature. The dashed line comes from the linear fits to extract the E_a from each exponential. (d) The natural logarithm of AF *versus* $1/k_BT$. The standard operating condition for AF value calculation is 1-sun illumination at 25 °C. (e) Light cycling tests of six encapsulated POTSC devices without and with poly-FPTS treatment under light on–off cycles test (12 hours-12 hours) using simulated 1-sun illumination at 23 ± 4 °C and 47 ± 5% RH (ISOS-LC-1).

after 1000 hours, far exceeding untreated devices. Encapsulated POTSCs were further tested under thermal stress using ISOS-L protocols (Note S6, SI). Untreated and poly-FPTS-treated devices were operated for over 1000 hours under 1-sun illumination at 45–85 °C. Initial *J–V* curves and optical images of encapsulated devices are provided in Fig. S40 and S41 (SI), respectively. Untreated devices maintained only 73.9% (45 °C) and 66.9% (65 °C) of their initial PCE after 400 hours, degrading to 55.4% at 85 °C within only 269 hours (Fig. 4b and Fig. S42, SI). In contrast, poly-FPTS-treated devices maintained 89.3% (45 °C), 83.1% (65 °C), and 68.8% (85 °C) PCE retention after 1000 hours, aligning with their superior thermal resilience.

We then calculated the E_a and acceleration factors (AFs) from temperature-dependent degradation data (Fig. 4c, 4d).[76,77] Poly-FPTS-treated POTSCs exhibited higher E_a (0.351 ± 0.049 eV) than controls (0.215 ± 0.033 eV), indicating greater resistance to thermal degradation. Using these AFs, we estimated equivalent operating times at a reference temperature of 25 °C by multiplying aging durations by the respective AFs. This dataset enabled T_{80} lifetime predictions for both tandems operating at 25 °C. Derived from E_a, the lifetime acceleration factor predicts poly-FPTS-treated devices will retain 80% PCE for over 4134 hours at 25 °C, significantly surpassing the 482 hours of untreated devices.

Further, we also investigated the light cycling stability of untreated and poly-FPTS-treated devices under continuous 1-sun illumination at room temperature by tracking their MPPs. The encapsulated POTSCs were subjected to light cycling tests under indoor conditions of 23 ± 4 °C and 47 ± 5% RH. As shown in Fig. 4e, the poly-FPTS-treated POTSCs show a slight efficiency decline of 4.7% after 1056 hours, whereas the untreated POTSCs lost 23.3% of their initial efficiency.

Conclusions

In summary, we demonstrated a multidentate anchoring-bridging strategy to fabricate highly efficient and stable POTSCs exhibiting a PCE of 26.5% and operational stability (T_{92} > 1000 h) *via* interface modification using coupling FPTS. Through the in-depth analysis of surface interaction, ionic migration kinetics, and the evolution of optoelectronic properties, it was elucidated that the poly-FPTS network can suppress the migration of mobile halide ions and homogenize the interfacial energy landscape, thereby improving device efficiency and long-term stability. This breakthrough in POTSC performance reveals the potential of multidentate coordination strategies toward commercially viable and highly efficient perovskite-based tandem solar cells.

Author contributions

Z. Z. conceived the ideas and designed the project while also providing guidance and supervision for research. D. Z. fabricated the devices, conducted the characterization, and analyzed the data. D. Z., B. L., D. G., X. S., N. K., F. V., X. W., S. L., J. G., L. W., Y. B., S. X., and M. S. contributed to the characterization and data analysis. B. L., X. W., Y. W., and W. T. also contributed to the fabrication of devices. Q. L. and X. C. Z. conducted DFT calculations. B. L., D. G., X. S., Z. Y., C. Z., N. W., Y. W., M. S., X. C. Z., S. Y. and Z. Z. supervised the writing and revision of the manuscript. All authors contributed to the manuscript revision.

Conflicts of interest

There are no conflicts to declare.

Data availability

The data supporting this article have been included as part of the supplementary information (SI). Supplementary information is available. See DOI: https://doi.org/10.1039/d5ee06253e.

Acknowledgements

The work was supported by National Natural Science Foundation of China (52322318), Research Grants Council of Hong Kong Grant (RFS2526-1S02, R1001-24F, C1055-23G, CRS_CityU104/24, 11308125, N_CityU102/23, 11306521, 11300124, C4005-22Y), Innovation and Technology Fund (ITS/147/22FP, MHP/079/23), the Science Technology and Innovation Committee of Shenzhen Municipality (JCYJ20220818101018038), National Key Research and Development Program of China (No. 2023YFB3809700).

References

1 Z. Jia, X. Guo, X. Yin, M. Sun, J. Qiao, X. Jiang, X. Wang, Y. Wang, Z. Dong, Z. Shi, C.-H. Kuan, J. Hu, Q. Zhou, X. Jia, J. Chen, Z. Wei, S. Liu, H. Liang, N. Li, L. K. Lee, R. Guo, S. V. Roth, P. Müller-Buschbaum, X. Hao, X. Du and Y. Hou, *Nature*, 2025, **643**, 104–110.

2 X. Jiang, S. Qin, L. Meng, G. He, J. Zhang, Y. Wang, Y. Zhu, T. Zou, Y. Gong, Z. Chen, G. Sun, M. Liu, X. Li, F. Lang and Y. Li, *Nature*, 2024, **635**, 860–866.

3 L. Jia, S. Xia, J. Li, Y. Qin, B. Pei, L. Ding, J. Yin, T. Du, Z. Fang, Y. Yin, J. Liu, Y. Yang, F. Zhang, X. Wu, Q. Li, S. Zhao, H. Zhang, Q. Li, Q. Jia, C. Liu, X. Gu, B. Liu, X. Dong, J. Liu, T. Liu, Y. Gao, M. Yang, S. Yin, X. Ru, H. Chen, B. Yang, Z. Zheng, W. Zhou, M. Dou, S. Wang, S. Gao, L. Chen, M. Qu, J. Lu, L. Fang, Y. Wang, H. Deng, J. Yu, X. Zhang, M. Li, X. Lang, C. Xiao, Q. Hu, C. Xue, L. Ning, Y. He, Z. Li, X. Xu and B. He, *Nature*, 2025, **644**, 912–919.

4 Z. Liu, R. Lin, M. Wei, M. Yin, P. Wu, M. Li, L. Li, Y. Wang, G. Chen, V. Carnevali, L. Agosta, V. Slama, N. Lempesis, Z. Wang, M. Wang, Y. Deng, H. Luo, H. Gao, U. Rothlisberger, S. M. Zakeeruddin, X. Luo, Y. Liu, M. Grätzel and H. Tan, *Nat. Mater.*, 2025, 1–8.

5 L. Wang, N. Wang, X. Wu, B. Liu, Q. Liu, B. Li, D. Zhang, N. Kalasariya, Y. Zhang, X. Yan, J. Wang, P. Zheng, J. Yang, H. Jin, C. Wang, L. Qian, B. Yang, Y. Wang, X. Cheng, T. Song, M. Stolterfoht, X. C. Zeng, X. Zhang, M. Xu, Y. Bai, F. Xu, C. Zhou and Z. Zhu, *Adv. Mater.*, 2025, **37**, 2416150.

6 X. Li, S. Gao, X. Wu, Q. Liu, L. Zhu, C. Wang, Y. Wang, Z. Liu, W. Chen, X. Li, P. Xiao, Q. Huang, T. Chen, Z. Li, X. Gao, Z. Xiao, Y. Lu, X. Zeng, S. Xiao, Z. Zhu and S. Yang, *Joule*, 2024, **8**, 3169–3185.

7 C. Zhang, Z. Yu, B. Li, X. Li, D. Gao, X. Wu and Z. Zhu, *ACS Nano*, 2024, **18**, 32299–32314.

8 K. O. Brinkmann, P. Wang, F. Lang, W. Li, X. Guo, F. Zimmermann, S. Olthof, D. Neher, Y. Hou, M. Stolterfoht, T. Wang, A. B. Djurišić and T. Riedl, *Nat. Rev. Mater.*, 2024, **9**, 202–217.

9 Z. Zhang, W. Chen, X. Jiang, J. Cao, H. Yang, H. Chen, F. Yang, Y. Shen, H. Yang, Q. Cheng, X. Chen, X. Tang, S. Kang, X. Ou, C. J. Brabec, Y. Li and Y. Li, *Nat. Energy*, 2024, **9**, 592–601.

10 S. Wu, Y. Yan, J. Yin, K. Jiang, F. Li, Z. Zeng, S.-W. Tsang and A. K.-Y. Jen, *Nat. Energy*, 2024, **9**, 411–421.

11 X. Wang, D. Zhang, B. Liu, X. Wu, X. Jiang, S. Zhang, Y. Wang, D. Gao, L. Wang, H. Wang, Z. Huang, X. Xie, T. Chen, Z. Xiao, Q. He, S. Xiao, Z. Zhu and S. Yang, *Adv. Mater.*, 2023, **35**, 2305946.

12 X. Wu, D. Zhang, B. Liu, Y. Wang, X. Wang, Q. Liu, D. Gao, N. Wang, B. Li, L. Wang, Z. Yu, X. Li, S. Xiao, N. Li, M. Stolterfoht, Y.-H. Lin, S. Yang, X. C. Zeng and Z. Zhu, *Adv. Mater.*, 2024, **36**, 2410692.
13 Y. Wang, B. Liu, D. Zhang, H. Yu, X. Wu, D. Gao, B. Li, C. Zhang, W. Liu, Z. Yu, N. Wang, L. Wang, X. Li, H. Yan and Z. Zhu, *Small*, 2025, **21**, 2411031.
14 H. Yu, Y. Wang, C. H. Kwok, R. Zhou, Z. Yao, S. Mukherjee, A. Sergeev, H. Hu, Y. Fu, H. M. Ng, L. Chen, D. Zhang, D. Zhao, Z. Zheng, X. Lu, H. Yin, K. S. Wong, H. Ade, C. Zhang, Z. Zhu and H. Yan, *Joule*, 2024, **8**, 2304–2324.
15 W. Liu, H. Yu, B. Liu, Y. Wang, H. Hu, H. M. Ng, C. H. Kwok, J. Yi, C. Zhang, F. Huang, Z. Zhu and H. Yan, *Adv. Funct. Mater.*, 2024, **34**, 2400131.
16 Y. Wang, H. Yu, D. Zhao, W. Liu, B. Liu, X. Wu, D. Gao, D. Zhang, S. Zhang, X. Sun, C. Zhang, C. Zhao, Y. Fu, W. Song, S. Gong, Y. Fu, C. H. Kwok, Z. Ge, X. Lu, X. Chen, S. Xiao, W.-Y. Wong, Y. Chai, H. Yan and Z. Zhu, *Adv. Energy Mater.*, 2025, 2404499.
17 H. Wang, Q. Li, Y. Zhu, X. Sui, X. Fan, M. Lin, Y. Shi, Y. Zheng, H. Yuan, Y. Zhou, H. Jin, H. G. Yang, Y. Hou and S. Yang, *Energy Environ. Sci.*, 2025, **18**, 2254–2263.
18 B. Li, S. Li, J. Gong, X. Wu, Z. Li, D. Gao, D. Zhao, C. Zhang, Y. Wang and Z. Zhu, *Chem*, 2024, **10**, 35–47.
19 H. Zhu, S. Teale, M. N. Lintangpradipto, S. Mahesh, B. Chen, M. D. McGehee, E. H. Sargent and O. M. Bakr, *Nat. Rev. Mater.*, 2023, **8**, 569–586.
20 A. J. Ramadan, R. D. J. Oliver, M. B. Johnston and H. J. Snaith, *Nat. Rev. Mater.*, 2023, **8**, 822–838.
21 Z. Yu, C. Zhang, B. Li, X. Wu, X. Li, D. Gao and Z. Zhu, *ACS Energy Lett.*, 2024, **9**, 5810–5821.
22 Z. Guo, A. K. Jena, G. M. Kim and T. Miyasaka, *Energy Environ. Sci.*, 2022, **15**, 3171–3222.
23 Y. Zhou, I. Poli, D. Meggiolaro, F. De Angelis and A. Petrozza, *Nat. Rev. Mater.*, 2021, **6**, 986–1002.
24 S. L. Choon and H. N. Lim, *Mater. Today Energy*, 2024, **43**, 101577.
25 Y. Zhao, W. Zhou, Z. Han, D. Yu and Q. Zhao, *Phys. Chem. Chem. Phys.*, 2021, **23**, 94–106.
26 Y.-C. Zhao, W.-K. Zhou, X. Zhou, K.-H. Liu, D.-P. Yu and Q. Zhao, *Light: Sci. Appl.*, 2017, **6**, e16243.
27 X. Sun, C. Zhang, D. Gao, S. Zhang, B. Li, J. Gong, S. Li, S. Xiao, Z. Zhu and Z. Li, *Adv. Funct. Mater.*, 2024, **34**, 2315157.
28 X. Luo, D. Gao, D. Zhang, G. Zhou, Y. Guo, C. Zhang, Z. Zhu and B. Xu, *Adv. Funct. Mater.*, 2025, **35**, 2425038.
29 F. Vanin, W. D. J. Tremlett, D. Gao, Q. Liu, B. Li, S. Li, J. Gong, X. Wu, Z. Li, R. K. Brown, L. Qian, C. Zhang, X. Sun, X. Li, X. C. Zeng, Z. Zhu and N. J. Long, *Angew. Chem., Int. Ed.*, 2025, **64**, e202424041.
30 X. Yu, X. Sun, Z. Zhu and Z. Li, *Angew. Chem., Int. Ed.*, 2025, **64**, e202419608.
31 B. Li, C. Zhang, D. Gao, X. Sun, S. Zhang, Z. Li, J. Gong, S. Li and Z. Zhu, *Adv. Mater.*, 2024, **36**, 2309768.
32 X. Sun, C. Zhang, D. Gao, X. Yu, B. Li, X. Wu, S. Zhang, Y. He, Z. Yu, L. Qian, J. Gong, S. Li, N. Li, Z. Zhu and Z. Li, *Angew. Chem.*, 2025, **137**, e202412819.
33 D. Valli, H. Zhang, M. Betušiak, G. Romolini, A. Meulemans, D. Escudero, S. Seth, Q. Zhao, Z. Zhu, M. Bonn, E. Belas, R. Grill, H. Wang, J. Hofkens and E. Debroye, *ACS Appl. Opt. Mater.*, 2024, **2**, 2075–2084.
34 X. Jiang, B. Liu, X. Wu, S. Zhang, D. Zhang, X. Wang, S. Gao, Z. Huang, H. Wang, B. Li, Z. Xiao, T. Chen, A. K.-Y. Jen, S. Xiao, S. Yang and Z. Zhu, *Adv. Mater.*, 2024, **36**, 2313524.
35 Y. Guo, F. Yao, Y. Zhang, G. Chen, S. Du, Z. Yu, H. Zhou, W. Ke, C. Li and G. Fang, *Energy Environ. Sci.*, 2025, **18**, 4916–4924.
36 X. Li, X. Wu, B. Li, Z. Cen, Y. Shang, W. Lian, R. Cao, L. Jia, Z. Li, D. Gao, X. Jiang, T. Chen, Y. Lu, Z. Zhu and S. Yang, *Energy Environ. Sci.*, 2022, **15**, 4813–4822.
37 W. Zhou, J. Gu, Z. Yang, M. Wang and Q. Zhao, *J. Phys. Appl. Phys.*, 2020, **54**, 063001.
38 B. Zhang, Y. Liao, L. Tong, Y. Yang and X. Wang, *Phys. Chem. Chem. Phys.*, 2020, **22**, 7778–7786.
39 X. Feng, B. Liu, Y. Peng, C. Gu, X. Bai, M. Long, M. Cai, C. Tong, L. Han and J. Yang, *Small*, 2022, **18**, 2201831.
40 S. Yang, S. Chen, E. Mosconi, Y. Fang, X. Xiao, C. Wang, Y. Zhou, Z. Yu, J. Zhao, Y. Gao, F. De Angelis and J. Huang, *Science*, 2019, **365**, 473–478.
41 Y. Wang, T. Wu, J. Barbaud, W. Kong, D. Cui, H. Chen, X. Yang and L. Han, *Science*, 2019, **365**, 687–691.
42 X. Li, W. Zhang, X. Guo, C. Lu, J. Wei and J. Fang, *Science*, 2022, **375**, 434–437.
43 J. Li, X. Qiao, B. He, Y. Zhang, S. Pal, L. Sun, M. Bilal, Z. Su, X. Gao, J. Briscoe, I. Abrahams, M. Li, Z. Li and Y. Lu, *Energy Environ. Sci.*, 2025, **18**, 5632–5642.
44 M. Lu, J. Ding, Q. Ma, Z. Zhang, M. Li, W. Gao, W. Mo, B. Zhang, T. Pauporté, J. Zhang, Y. Wang, J.-X. Tang, J. Chen and C. Chen, *Energy Environ. Sci.*, 2025, **18**, 5973–5984.
45 H. Chen, C. Liu, J. Xu, A. Maxwell, W. Zhou, Y. Yang, Q. Zhou, A. S. R. Bati, H. Wan, Z. Wang, L. Zeng, J. Wang, P. Serles, Y. Liu, S. Teale, Y. Liu, M. I. Saidaminov, M. Li, N. Rolston, S. Hoogland, T. Filleter, M. G. Kanatzidis, B. Chen, Z. Ning and E. H. Sargent, *Science*, 2024, **384**, 189–193.
46 S. M. Park, M. Wei, J. Xu, H. R. Atapattu, F. T. Eickemeyer, K. Darabi, L. Grater, Y. Yang, C. Liu, S. Teale, B. Chen, H. Chen, T. Wang, L. Zeng, A. Maxwell, Z. Wang, K. R. Rao, Z. Cai, S. M. Zakeeruddin, J. T. Pham, C. M. Risko, A. Amassian, M. G. Kanatzidis, K. R. Graham, M. Grätzel and E. H. Sargent, *Science*, 2023, **381**, 209–215.
47 H. Chen, S. Teale, B. Chen, Y. Hou, L. Grater, T. Zhu, K. Bertens, S. M. Park, H. R. Atapattu, Y. Gao, M. Wei, A. K. Johnston, Q. Zhou, K. Xu, D. Yu, C. Han, T. Cui, E. H. Jung, C. Zhou, W. Zhou, A. H. Proppe, S. Hoogland, F. Laquai, T. Filleter, K. R. Graham, Z. Ning and E. H. Sargent, *Nat. Photonics*, 2022, **16**, 352–358.
48 C. A. R. Perini, E. Rojas-Gatjens, M. Ravello, A.-F. Castro-Mendez, J. Hidalgo, Y. An, S. Kim, B. Lai, R. Li, C. Silva-Acuña and J.-P. Correa-Baena, *Adv. Mater.*, 2022, **34**, 2204726.
49 K. Ma, H. R. Atapattu, Q. Zhao, Y. Gao, B. P. Finkenauer, K. Wang, K. Chen, S. M. Park, A. H. Coffey, C. Zhu,

L. Huang, K. R. Graham, J. Mei and L. Dou, *Adv. Mater.*, 2021, **33**, 2100791.
50 Z. Li, B. Li, X. Wu, S. A. Sheppard, S. Zhang, D. Gao, N. J. Long and Z. Zhu, *Science*, 2022, **376**, 416–420.
51 D. Gao, B. Li, X. Sun, Q. Liu, C. Zhang, L. Qian, Z. Yu, X. Li, X. Wu, B. Liu, N. Wang, F. Vanin, X. Xia, J. Gong, N. Li, X. C. Zeng, Z. Li and Z. Zhu, *Nat. Photonics*, 2025, **19**, 1070–1077.
52 A. I. A. Soliman, Y. Zhang, L. Zhang, H. Wu, S. Shan, Y. Zhou, C. Xu, W. Fu and H. Chen, *Adv. Funct. Mater.*, 2025, **35**, 2412886.
53 Y.-H. Lin, Vikram, F. Yang, X.-L. Cao, A. Dasgupta, R. D. J. Oliver, A. M. Ulatowski, M. M. McCarthy, X. Shen, Q. Yuan, M. G. Christoforo, F. S. Y. Yeung, M. B. Johnston, N. K. Noel, L. M. Herz, M. S. Islam and H. J. Snaith, *Science*, 2024, **384**, 767–775.
54 Y. Shi, E. Rojas-Gatjens, J. Wang, J. Pothoof, R. Giridharagopal, K. Ho, F. Jiang, M. Taddei, Z. Yang, E. M. Sanehira, M. D. Irwin, C. Silva-Acuña and D. S. Ginger, *ACS Energy Lett.*, 2022, **7**, 4081–4088.
55 R. Lin, J. Xu, M. Wei, Y. Wang, Z. Qin, Z. Liu, J. Wu, K. Xiao, B. Chen, S. M. Park, G. Chen, H. R. Atapattu, K. R. Graham, J. Xu, J. Zhu, L. Li, C. Zhang, E. H. Sargent and H. Tan, *Nature*, 2022, **603**, 73–78.
56 Y. Wang, R. Lin, C. Liu, X. Wang, C. Chosy, Y. Haruta, A. D. Bui, M. Li, H. Sun, X. Zheng, H. Luo, P. Wu, H. Gao, W. Sun, Y. Nie, H. Zhu, K. Zhou, H. T. Nguyen, X. Luo, L. Li, C. Xiao, M. I. Saidaminov, S. D. Stranks, L. Zhang and H. Tan, *Nature*, 2024, **635**, 867–873.
57 B. Li, Y. Cai, X. Tian, X. Liang, D. Li, Z. Zhang, S. Wang, K. Guo and Z. Liu, *J. Energy Chem.*, 2021, **62**, 523–531.
58 Q. Yang, X. Zhang, S. Wang, X. Han, Y. Gu, X. Bi, D. Chen, W. Fang and B. Liu, *Appl. Surf. Sci.*, 2024, **659**, 159925.
59 H. B. Lee, N. Kumar, V. Devaraj, B. Tyagi, S. He, R. Sahani, K.-J. Ko, J.-W. Oh and J.-W. Kang, *Sol. RRL*, 2021, **5**, 2100712.
60 Y. Wang, Y. Feng, H. Yang, S. Li, K. Zhang, Y. Feng, X. Han, T. Alshahrani, Q. An, X. Wang, H. Li, Y. Jiang and M. Yuan, *Adv. Mater.*, 2025, e07730.
61 T. Xu, W. Xiang, X. Ru, Z. Wang, Y. Liu, N. Li, H. Xu and S. Liu, *Adv. Mater.*, 2024, **36**, 2312237.
62 Z. Li, J. Guo, Z. Li, W. Han, G. Ren, C. Liu, L. Shen and W. Guo, *J. Mater. Chem. A*, 2020, **8**, 5629–5637.
63 J. Thiesbrummel, S. Shah, E. Gutierrez-Partida, F. Zu, F. Peña-Camargo, S. Zeiske, J. Diekmann, F. Ye, K. P. Peters, K. O. Brinkmann, P. Caprioglio, A. Dasgupta, S. Seo, F. A. Adeleye, J. Warby, Q. Jeangros, F. Lang, S. Zhang, S. Albrecht, T. Riedl, A. Armin, D. Neher, N. Koch, Y. Wu, V. M. Le Corre, H. Snaith and M. Stolterfoht, *Nat. Energy*, 2024, **9**, 664–676.
64 V. M. Le Corre, J. Diekmann, F. Peña-Camargo, J. Thiesbrummel, N. Tokmoldin, E. Gutierrez-Partida, K. P. Peters, L. Perdigón-Toro, M. H. Futscher, F. Lang, J. Warby, H. J. Snaith, D. Neher and M. Stolterfoht, *Sol. RRL*, 2022, **6**, 2100772.
65 F. Akrami, F. Jiang, R. Giridharagopal and D. S. Ginger, *J. Phys. Chem. Lett.*, 2023, **14**, 9310–9315.
66 Y. Hou, E. Aydin, M. De Bastiani, C. Xiao, F. H. Isikgor, D.-J. Xue, B. Chen, H. Chen, B. Bahrami, A. H. Chowdhury, A. Johnston, S.-W. Baek, Z. Huang, M. Wei, Y. Dong, J. Troughton, R. Jalmood, A. J. Mirabelli, T. G. Allen, E. Van Kerschaver, M. I. Saidaminov, D. Baran, Q. Qiao, K. Zhu, S. De Wolf and E. H. Sargent, *Science*, 2020, **367**, 1135–1140.
67 T.-X. Qin, E.-M. You, M.-X. Zhang, P. Zheng, X.-F. Huang, S.-Y. Ding, B.-W. Mao and Z.-Q. Tian, *Light: Sci. Appl.*, 2021, **10**, 84.
68 B. Li, X. Wu, S. Zhang, Z. Li, D. Gao, X. Chen, S. Xiao, C.-C. Chueh, A. K.-Y. Jen and Z. Zhu, *Chem. Eng. J.*, 2022, **446**, 137144.
69 Z. Zhu, K. Mao, K. Zhang, W. Peng, J. Zhang, H. Meng, S. Cheng, T. Li, H. Lin, Q. Chen, X. Wu and J. Xu, *Joule*, 2022, **6**, 2849–2868.
70 B. Li, D. Gao, S. A. Sheppard, W. D. J. Tremlett, Q. Liu, Z. Li, A. J. P. White, R. K. Brown, X. Sun, J. Gong, S. Li, S. Zhang, X. Wu, D. Zhao, C. Zhang, Y. Wang, X. C. Zeng, Z. Zhu and N. J. Long, *J. Am. Chem. Soc.*, 2024, **146**, 13391–13398.
71 B. Li, Q. Liu, J. Gong, S. Li, C. Zhang, D. Gao, Z. Chen, Z. Li, X. Wu, D. Zhao, Z. Yu, X. Li, Y. Wang, H. Lu, X. C. Zeng and Z. Zhu, *Nat. Commun.*, 2024, **15**, 2753.
72 M. A. Green, E. D. Dunlop, M. Yoshita, N. Kopidakis, K. Bothe, G. Siefer, X. Hao and J. Y. Jiang, *Prog. Photovolt. Res. Appl.*, 2025, **33**, 3–15.
73 J. Wang, J. Zhang, Y. Zhou, H. Liu, Q. Xue, X. Li, C.-C. Chueh, H.-L. Yip, Z. Zhu and A. K. Y. Jen, *Nat. Commun.*, 2020, **11**, 177.
74 M. V. Khenkin, E. A. Katz, A. Abate, G. Bardizza, J. J. Berry, C. Brabec, F. Brunetti, V. Bulović, Q. Burlingame, A. Di Carlo, R. Cheacharoen, Y.-B. Cheng, A. Colsmann, S. Cros, K. Domanski, M. Dusza, C. J. Fell, S. R. Forrest, Y. Galagan, D. Di Girolamo, M. Grätzel, A. Hagfeldt, E. von Hauff, H. Hoppe, J. Kettle, H. Köbler, M. S. Leite, S. (Frank) Liu, Y.-L. Loo, J. M. Luther, C.-Q. Ma, M. Madsen, M. Manceau, M. Matheron, M. McGehee, R. Meitzner, M. K. Nazeeruddin, A. F. Nogueira, Ç. Odabaşı, A. Osherov, N.-G. Park, M. O. Reese, F. De Rossi, M. Saliba, U. S. Schubert, H. J. Snaith, S. D. Stranks, W. Tress, P. A. Troshin, V. Turkovic, S. Veenstra, I. Visoly-Fisher, A. Walsh, T. Watson, H. Xie, R. Yıldırım, S. M. Zakeeruddin, K. Zhu and M. Lira-Cantu, *Nat. Energy*, 2020, **5**, 35–49.
75 D. Gao, B. Li, Q. Liu, C. Zhang, Z. Yu, S. Li, J. Gong, L. Qian, F. Vanin, K. Schutt, M. A. Davis, A. F. Palmstrom, S. P. Harvey, N. J. Long, J. M. Luther, X. C. Zeng and Z. Zhu, *Science*, 2024, **386**, 187–192.
76 X. Zhao, T. Liu, Q. C. Burlingame, T. Liu, R. Holley, G. Cheng, N. Yao, F. Gao and Y.-L. Loo, *Science*, 2022, **377**, 307–310.
77 Z. Li, X. Sun, X. Zheng, B. Li, D. Gao, S. Zhang, X. Wu, S. Li, J. Gong, J. M. Luther, Z. Li and Z. Zhu, *Science*, 2023, **382**, 284–289.

